Modeling, Force Sensing, and Control of Flexible Cannulas for Microstent Delivery

Wei Wei
e-mail: ww2161@columbia.edu

Nabil Simaan[1]
e-mail: nabil.simaan@vanderbilt.edu

Advanced Robotics and Mechanisms, Applications Lab (ARMA Lab), Department of Mechanical Engineering, Vanderbilt University, Nashville, TN 37240

This paper presents a kinetostatic modeling framework for flexible cannulas (concentric tubing robots) subject to tip loads. Unlike existing methods that allow fast computation of the beam tip position, this modeling framework provides fast computation of both the tip position and the entire shape of the deflected robot. A method for online force sensing based on inverse kinetostatic solution is also proposed and assistive telemanipulation control methods for microstent delivery are presented. The modeling framework uses polynomial approximation and linear interpolation based on elliptic integral solutions to the deflection of lightweight beams. To date, there are no systems capable of stent delivery in retinal vasculature. The modeling and control frameworks of this paper are validated experimentally on pilot studies for microstent delivery. We believe that the methods presented in this paper open the way for robot-assisted retinal microvascular stenting that may potentially revolutionize the treatment of blinding retinal vasculature diseases.
[DOI: 10.1115/1.4006080]

1 Introduction

Steerable cannula robots are composed of flexible tubes and possibly guide wires. These robots provide excellent miniaturization and support a variety of high-impact medical applications such as drug delivery, prostate brachytherapy, catheterization, and transcutaneous biopsy. Steerability of flexible cannulas may be achieved in a variety of ways. For example, robotic steerable insertion of needles was shown to be controllable by variable insertion speed and axial rotation of a needle inside the tissue [1], by controlled insertion coupled with a variable duty cycle spinning of a beveled tip needle [2], and by changing the boundary conditions of the needles during transcutaneous biopsy [3]. If, however, one wishes to actively control a steerable cannula, the design includes multiple concentric NiTi tubes with preshaped segments. By stacking these segments in a concentric manner, an equilibrium 3D shape may be achieved and controlled either by changing the insertion of one tube inside another or by rotating one tube with respect to another. Early examples of this approach were presented in Ref. [4] for a hand-held biopsy device with one preshaped sheath and a flexible needle. More complex designs were almost simultaneously explored by Sears and Dupont [5] and Webster et al. [6] using stacked concentric NiTi tubes with preshaped circular segments. In the past 5 years there have been several works on statics modeling [7,8], vibration [9], inverse kinematics [10], insertion path planning [11,12], image guidance [13], and telemanipulation [14].

Though kinematics and equilibrium conformations of concentric tubing robots (CTRs) have been presented [1,5,6,10], a fast solution to the statics and updated kinematics has not been presented. Xu and Simaan[15] used elliptic integrals as an extension of the work [16] to model the statics of continuum robots with multiple flexible backbones. Due to its cumbersome formulation, use of elliptic integrals is not common in actual practices, and numerical approaches have been proposed to approximate deflections of a cantilever beam.

Finite element analysis [17,18] was useful for modeling and simulating large deformation of cantilever beams under different loading conditions. Extended Lagrangian optimization method [19] was used to solve equilibrium shapes of linear flexible objects, but the iterative solution required a computation time of 17.6 s. Other works such as homotopy analysis method [20] and shooting method [21] also suffer from iterative computations and therefore are not appropriate for real-time control. Pseudo-rigid-body model (PRBM) [22] was proposed to approximate the motion of the tip of a flexible beam with pseudo rigid bodies connected by imaginary torsional spring joints. The work [23] extended the PRBM model to 3R and solved large deflection problems. Although PRBM has simple expressions and does not require iteration, the solution only gives the deflected tip coordinates but not the shape of the entire beam. Fertis [24] presented an iterative solution method using pseudo-linear beam models to solve for the beam shape, which is not suitable for real-time control of robots, either.

The approach presented in this paper is based on an understanding of the elliptic integral solution to the deflection of a beam. The fundamental observation behind our work is that a given beam with a known length and a known direction of a tip force and a desired tip deflection angle assumes a single shape as determined by the elliptic integral solution. Further, the magnitude of the force is not independent from the direction of the force and the equilibrium beam tip angle. Based on this observation, the problem of solving the beam shape and a framework for force sensing are derived using an interpolation approach that is easy to program for robot control.

The approach presented here is essentially similar to using a lookup table but has the added advantage of being based on an understanding of the underlying mechanics of the beam rather than using brute force precomputation of equilibrium beam shapes.

In Ref. [25], we simplified the structure of a tubing robot as rigid body links connected by imaginary revolute joints. The derived Jacobian treated the whole robotic system as rigid and did not take the flexibility of the CTR into account. In this paper, the actual deflection of the flexible beam is considered while we formulate the Jacobian for the CTR. Webster and Dupont derived the Jacobian of CTR for no-load case [8,10]. The result was good enough for applications where the effects of the loads were negligible. However, for our potential application in ophthalmic surgery, due to the slenderness of the tube components, contact forces between the robot and the environment will generate

[1]Corresponding author.

Contributed by the Dynamic Systems Division of ASME for publication in the JOURNAL OF DYNAMIC SYSTEMS, MEASUREMENT, AND CONTROL. Manuscript received July 7, 2010; final manuscript received January 10, 2012; published online April 26, 2012. Assoc. Editor: Marco P. Schoen.

significant deflection. Therefore, the robot deflection due to external loads will be formulated into our Jacobian derivation.

The contribution of this paper is twofold. First, the paper presents an analysis method for the computation of the shape of CTR with loads at the tip. The method lends itself to real-time control applications. Second, the paper presents an algorithm for force sensing capabilities by monitoring the tip deflection and position of a CTR. A motivating novel application for microvascular surgery is presented with explanation on the planned surgical setup.

Section 2 presents the clinical motivation behind this work, the corresponding theoretical problem statements, and the assumptions; Sec. 3 presents normalized flexible beam modeling; Sec. 4 presents the Jacobian formulation and control strategies for different applications; Sec. 5 presents the statics of the robot and its potential use as a force sensor; Sec. 6 presents the experimental results followed by Sec. 7 of conclusions.

2 Clinical Motivation and Problem Statement

2.1 Clinical Motivation. In ophthalmic surgery, two surgeons coordinate to perform surgical procedures, Fig. 1(*a*). The main surgeon sits superior to the patient's head and performs most of the surgical tasks including manipulation of the surgical instruments and the light source. The assistant surgeon sits beside the patient's head to provide irrigation and removal of fluids and to adjust the placement of external visualization lenses. Three incisions are typically made in the sclera to provide access to the vitreous body for an irrigation tube, a surgical instrument, and a light source, Fig. 1(*b*). The surgeons operate using a microscope while visualizing the retina through a dilated iris. Because the visual field does not contain the entire retinal surface, procedures often require tilting the eye under the microscope in order to view the peripheral areas of the retina.

The limitations of the current ophthalmic surgical setup include the lack of distal dexterity inside the eye, limited ability to perform precise coordinated bimanual operations, lack of precise stabilization, and manipulation of the eye itself under the microscope. In addition to the requirement for high precision, ophthalmic surgeons also face challenges stemming from deficient depth perception and the lack of force feedback. Only highly experienced surgeons can perform demanding retinal procedures such as membrane peeling.

In Ref. [25], we proposed a dual-arm system for robotic assistance in ophthalmic surgery, Fig. 2. This system is intended to address the challenges of precision, lack of intraocular dexterity, ocular manipulation, and bimanual coordination. Each arm of this system is composed of a six degrees-of-freedom (DoF) Stewart platform [26] and a 2-DoF intra-organ dexterity robot (IODR) on top of the parallel robot. The Stewart platform provides precise positioning of the IODR, while the IODR, designed as a CTR, is used to provide intra-ocular dexterity. Each individual arm is designed to perform dexterous operations such as retinal membrane peeling; the two arms can also be coordinated to tilt the eye

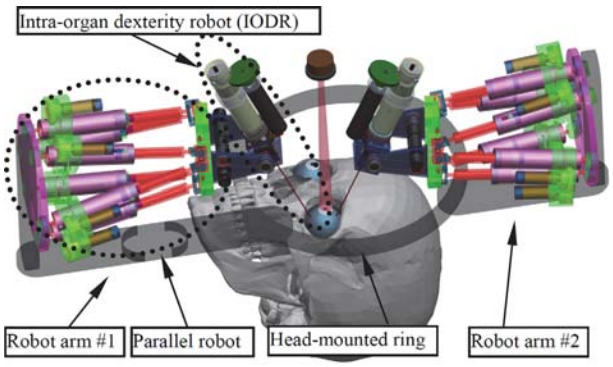

Fig. 2 A proposed dual-arm robotic system for ophthalmic surgery

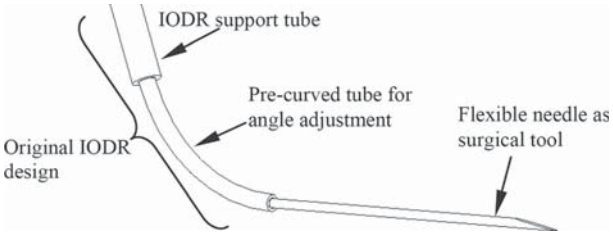

Fig. 3 Proposed concentric tubing robot for cannulation

for visualization and perform complex manipulations and operations simultaneously.

Despite previous works on retinal surgery, surgeons have not been able to perform microvascular stenting on the retina. This procedure has the potential to revolutionize ophthalmic surgery just as stenting did for cardiac applications. The motivation for microvascular stenting stems from the need for surgical treatment of vascular obstructions that lead to blindness in the case of central retinal vein occlusion (CRVO) and branch retinal vein occlusion (BRVO) [27–30]. Though pharmaceutical treatment may be able to resolve some obstruction, surgical treatment is needed for cases involving buckling of vasculature walls in vein-artery crossings.

To address these challenges, we propose a CTR as shown in Fig. 3. This modified design of the IODR can be customized as a surgical knife, a drug delivery tube, or controllable surgical forceps. In order to achieve successful control of this robot, there is a need for fast control and modeling algorithms that account for bending of the guide wire. In addition, this design has the potential to fill the gap of no force feedback in ophthalmic surgery when coupled with a kinetostatic modeling framework.

One potential application of the proposed robot shown in Fig. 3 is for drug delivery and cannulation. In this case, the flexible

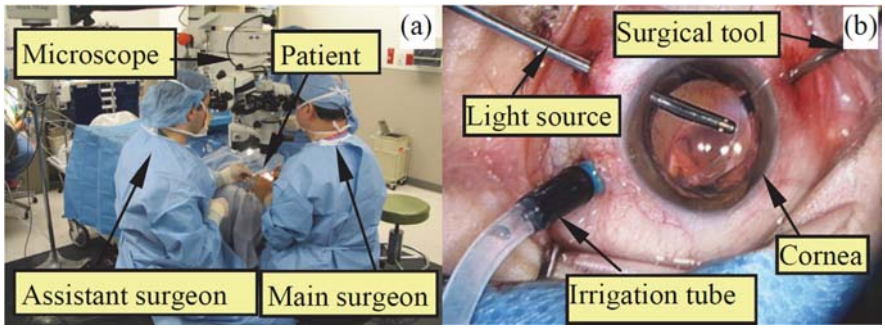

Fig. 1 A typical surgical setup for ophthalmic surgery

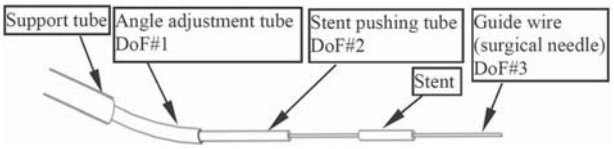

Fig. 4 Potential application of a concentric tubing robot as a microvascular stenting unit for retinal surgery

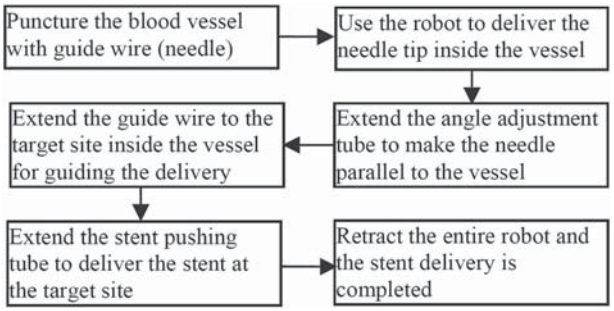

Fig. 5 Flowchart of stent delivery procedure using the proposed tubing robot

needle is made from a NiTi tube with a sharp tip for puncturing blood vessels. The precurved tube is used to adjust the approach angle of the cannula with respect to the retina. Another application is the surgical treatment of CRVO/BRVO—an obstruction to outflow of blood that leads to blindness. In this case, a stent-pushing tube is added between the precurved tube and the flexible needle, as shown in Fig. 4. The stent-pushing tube is used for pushing the stent axially along the guide wire inside the blood vessel. For the stenting application, the tubing robot has three DoFs. The work flow of a stent delivery procedure is as shown in Fig. 5.

2.2 Problem Statement and Simplifying Assumptions. Successful control of the CTR for ophthalmic surgical applications depends on the solution of three basic problems:

Problem 1. *Given the dimensions and material properties of an elastic beam, find a kinetostatic model that may be calculated fast enough for control purposes. The deflected shape of the beam subject to a known load is sought.*

Problem 2. *Derive an explicit expression for the deflection Jacobian of the CTR at a given configuration.*

Problem 3. *Given the location and orientation of the deflected beam tip, find a fast solution to the applied force at the tip of the beam.*

The solution to problem 1 provides an effective method for controlling flexible CTR subject to load. Though other works have presented fast solutions to the location and orientation of the beam tip, accurate control of CTR subject to external loads requires knowledge of their deflected shape. This solution contributes to providing a modeling framework for problem 2 that is essential for resolved-rate control. The solution to problem 3 provides a fast force feedback algorithm for CTR.

Several simplifying assumptions are made in order to facilitate solutions to problems 1–3:

Assumption 1. *The only force applied to the needle is applied at the tip and there is no moment applied.*

Assumption 2. *Our CTR design satisfies the conditions for dominating tube pairs as defined in Ref. [5]. The equilibrium shape of an unloaded dominating tube pair conforms to the shape of the dominating tube.*

Assumption 3. *The CTR has bounded deflections.*

Assumption 4. *Gravity effects are negligible.*

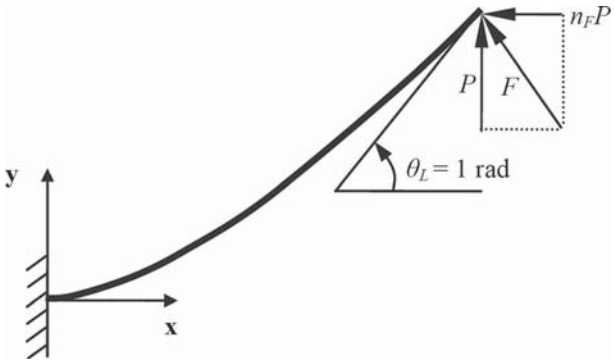

Fig. 6 Cantilever beam subject to a force applied at the distal tip

Assumption 5. *The CTR interacts with the retina such that the bending of the guide wire is in the same plane of the angle adjustment tube.*

Assumption 1 is justified in the case of ophthalmic surgery since the moments of interaction with the retina are negligible. In fact, most interactions involve point contact with the tip of surgical instruments. Assumption 2 is justified by our component selection for this CTR. The precurved NiTi tube has an OD of 0.55 mm and ID of 0.25 mm. For a drug delivery application, the inner tube has an OD of 0.2 mm and ID 0.1 mm. For a microstenting application, the needle/guide wire has a diameter of 0.07 mm. The stiffness ratios for both applications are calculated as 58 and 62, respectively. Hence, our robot is considered as dominating stiffness tube pairs. Assumption 3 is justified since the maximal deflection of a flexible surgical tool inside the limited workspace of the eyeball is expected to be always less than 60 deg. This guarantees that the cantilever beam is deflected only within a relatively small range. Assumption 4 is correct for small guide wires/beams that exhibit negligible deflection when placed horizontally. Finally, assumption 5 is justified since we assume that the external robot adjusting the CTR has sufficient DoF for meeting this condition.

3 Normalized Kinematic Modeling of a Cantilever Beam

A cantilever beam has one end clamped to the base and the other end free of constraints. Elliptic integral solutions for the shape of a beam subject to tip load have been presented by Howell [22]. The solutions from Ref. [22] have been summarized in Appendix for completeness.

3.1 Polynomial Approximation of Beam Deflection. Polynomial functions are proposed to be used for approximating the shape of a deflected cantilever beam. The same example as shown in Ref. [22] is used as a reference for this simulation. Assume a flexible beam is 100 mm long, with Young's modulus E of 71.7 GPa and moment of inertia I of $7.85 \times 10^{-13}\text{m}^4$. While subject to a tip load P in the y direction, the beam deflects to 1 rad, Fig. 6. Note that throughout this paper, the direction of the applied force is defined by n_F such that $n_F P$ denotes its horizontal component. For this specific example, $n_F = 0$. Note that in our derivation, only the force direction n_F but not the magnitude P is given.

According to the elliptic integral solution, the beam end point is deflected to (73.8 mm, 61.0 mm) and the applied force is 17.4 N. With known beam end position and tangent direction, the use of a third-order polynomial is proposed to approximate the shape of the deflected cantilever beam. Define a third-order polynomial as

$$y = c_3 x^3 + c_2 x^2 + c_1 x + c_0 \tag{1}$$

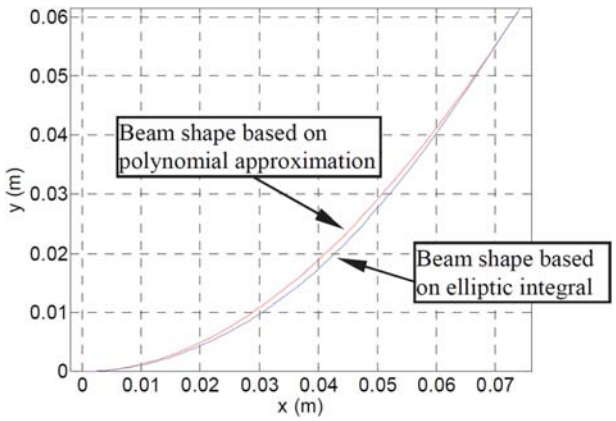

Fig. 7 Beam shape comparison of polynomial approximation and elliptic integral

Applying the boundary conditions (2) and (3) of beam ends position and orientation, we solve for the coefficients $c_0 \sim c_3$ as in Eq. (4).

$$y|_{x=0} = 0 \quad \text{and} \quad y|_{x=0.0738} = 0.061 \tag{2}$$

$$\left.\frac{dy}{dx}\right|_{x=0} = 0 \quad \text{and} \quad \left.\frac{dy}{dx}\right|_{x=0.0738} = \tan(1) \tag{3}$$

$$c_3 = -0.1759, \quad c_2 = 1.2495, \quad c_1 = c_0 = 0 \tag{4}$$

The solved third-order polynomial is plotted in the same frame with the elliptic integral solution of the beam shape as shown in Fig. 7, for comparison.

The position error, normalized by the beam length, is calculated for all corresponding points along the beam shapes given by the elliptic integral solution and the polynomial approximation. This normalized error is less than 1% for the example in Fig. 7. Given the third-order polynomial equation, curve integrations of Eqs. (5) and (6) were utilized to find the beam end point coordinates. In Eqs. (5) and (6), $\theta(s)$ denotes the intermediate deflection angle along the beam and is calculated from Eq. (7); L denotes the beam length.

$$x(s) = \int_0^s \cos(\theta(\tau))d\tau \tag{5}$$

$$y(s) = \int_0^s \sin(\theta(\tau))d\tau \tag{6}$$

$$\theta(s) = \tan^{-1}\left(\frac{dy}{dx}\right) \quad \text{where} \quad x = f^{-1}(s) \tag{7}$$

In Eq. (7), $x = f^{-1}(s)$ represents that given an intermediate beam length s, the x-coordinate of the corresponding beam point is to be solved through the inverse function of the curve integration along the third-order polynomial. Once having all the intermediate deflection angles $\theta(s)$ along the beam, the beam end point position can be obtained via integration. The numerical solution of the beam end point using curve integration was calculated to be (74.3 mm, 61.1 mm). A normalized position error of 0.5% is observed between the solutions by polynomial approximation and by elliptic integral (normalization was carried out with respect to beam length). This modeling accuracy of polynomial approximation is as good as using PRBM model [22] but provides a fast computation of all points along the deflected beam rather than only the tip position of the beam.

3.2 Length Preserving Shape Interpolation. Given two reference beam shapes characterized by functions $\theta_1(s)$ and $\theta_2(s)$, any interpolated shape $\theta(s,t)$ such that for $t=0$, $\theta(s,t)=\theta_1(s)$, and for $t=1$, $\theta(s,t)=\theta_2(s)$ is length-preserving since $\int_0^L \sqrt{\cos^2(\theta(s)) + \sin^2(\theta(s))}ds = L$. This length-preserving interpolation is to be used for creating an interpolated map for the equilibrium shapes of the beam subject to known load directions and tip deflection angles.

This approach lends itself for online computation of beam shapes subject to tip loading. The method uses the reference polynomials obtained from elliptic integral solutions as in the preceding section. Four reference polynomials (beam shapes) are presolved using elliptic integrals for a combination of two tip deflection angles with two force directions at the beam tip. Linear interpolation is carried out on the beam deflection angle and the applied force direction to solve for the target beam shape.

3.3 Normalized Beam Modeling Using Interpolation. Given two intervals, Eq. (8), for the beam tip deflection angle θ_L and the direction n_F of the applied force at the tip of a beam, an interpolation function $\theta(s, t_L, t_F)$ that provides the shape of the beam is sought. Two linear interpolation parameters t_L and t_F are calculated from Eqs. (9) and (10) for the corresponding deflection angles and force directions of the calculated reference beams.

$$\theta_L \in [\theta_{L\min}, \theta_{L\max}] \quad \text{and} \quad n_F \in [n_{F\min}, n_{F\max}] \tag{8}$$

$$\theta_L = (1-t_L)\theta_{L\min} + t_L\theta_{L\max} \quad (0 \le t_L \le 1) \tag{9}$$

$$n_F = (1-t_F)n_{F\min} + t_F n_{F\max} \quad (0 \le t_F \le 1) \tag{10}$$

Upon calculating all tangent angles of the reference beams from Eq. (7), the tangent angles of the target beam are interpolated as in Eq. (11). In Eq. (11), $t_{L\min}$ and $t_{F\min}$ are equal to 0 and $t_{L\max}$ and $t_{F\max}$ are equal to 1.

$$\begin{aligned}\theta(s,t_L,t_F) = (1-t_L)[(1-t_F)\theta(s,t_{L\min},t_{F\min}) + t_F\theta(s,t_{L\min},t_{F\max})] \\ + t_L[(1-t_F)\theta(s,t_{L\max},t_{F\min}) + t_F\theta(s,t_{L\max},t_{F\max})]\end{aligned} \tag{11}$$

Once $\theta(s, t_L, t_F)$ is solved, the target beam end point coordinates are obtained by integrating over the beam curve, as in Eqs. (5) and (6). Note that by changing the integration limit of Eqs. (5) and (6), this approach can quickly generate all point coordinates along the beam.

Figure 8 shows a simulation example of the proposed algorithm. The two interpolation intervals are selected as $[\theta_{L\min}, \theta_{L\max}] = [0.1, 1]$ rad for the deflection angle and $[n_{F\min}, n_{F\max}] = [0, 1]$ for the applied force direction. Hence, the applied force is within a 45 deg range.

To demonstrate our approach, assume that the tip deflection angle of an unknown beam shape is $\theta_L = 0.6$ rad and that the

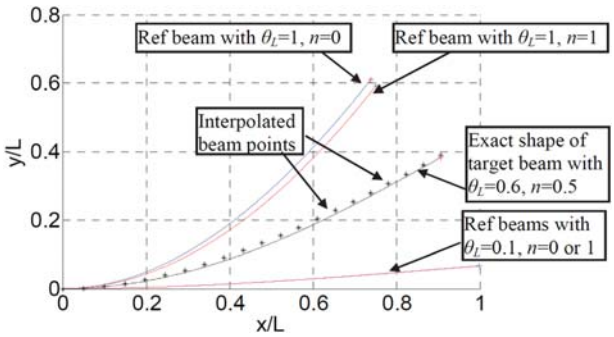

Fig. 8 Interpolation results of a cantilever beam under specified loading conditions. Dots in the middle are interpolated beam points, compared to the theoretical shape presented by the middle curve

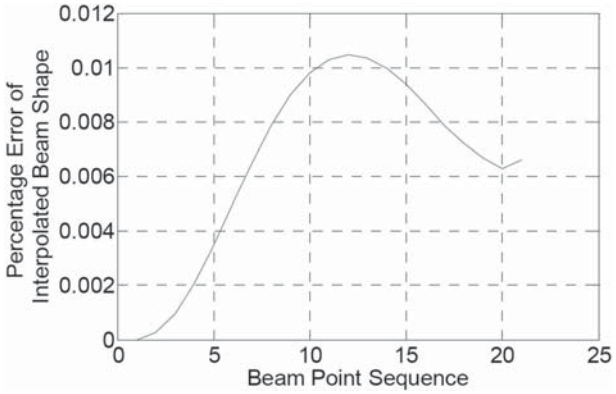

Fig. 9 Percentage error of the interpolated beam shape compared to the elliptic integral solution

applied force direction is $n_F = 0.5$. We use the interpolation Eqs. (9) and (10)) to find $t_L = 0.56$ and $t_F = 0.5$. Based on these interpolation factors, Eqs. (11), (5), and (6) are used to find the points along the unknown beam. These points are shown in Fig. 8 by star marks. The same figure also shows the reference beams generated off-line based on the polynomial approximation of the elliptic integral solutions. The exact beam shape based on elliptic integral solutions is also shown for the unknown beam. From the plot, we can see that these interpolated points agree well with the theoretical beam shape. Since in Fig. 8, all beam curves are normalized by the length of the beam, the proposed algorithm can be used to model cantilever beams with arbitrary lengths.

Figure 9 presents a numerical evaluation of the interpolation errors along the target beam. Using interpolation and curve integration results in an error that is less than 1.2% compared with the elliptic integral solution. Despite this error, the proposed approach is able to provide a fast model for the shape of the entire deflected beam and can be used for assistive telemanipulation control during stent insertion. Naturally, the fast interpolation method comes at a price of a small error. We believe that this small error is acceptable given that the user is kept in the loop during telemanipulation and for a beam that is 10 mm the error is less than 105 μm. Also, when the CTR is eventually integrated within a complete ophthalmic surgery system, calibration and visual servoing will mitigate these errors.

3.4 Computation Speed. We carried out simulations to compare the computation speed of our proposed interpolation method with elliptic integral solutions. The comparison was completed under MATLAB® environment on an Intel® Pentium® 4 computer with CPU speed 3.00 GHz and 2.00 G RAM. For both methods, we recorded the computation time for fully solving the entire beam shape by substituting Eq. (11) in Eqs. (5) and (6) for 1000 equally spaced values of $\theta(s) \in [0,\ \theta_L]$. For the elliptic integral solution, we used Eqs. (8) and (9) in Ref. [15] for the same 1000 equally spaced values of $\theta(s) \in [0,\ \theta_L]$.

Twenty groups of deflection angle and force direction were tested and reported in Table 1. For each beam tip angle, we varied the load direction by increments of 15 deg from 0 deg to 45 deg. From the results, we see that the interpolation method can satisfy online control requirement of 1 kHz; however, the elliptic integral method cannot be directly used because of the long computation time.

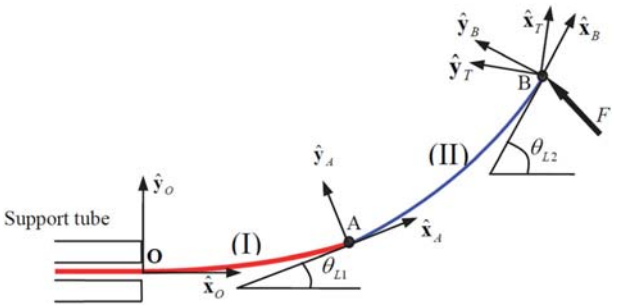

Fig. 10 Tubing robot force diagram

4 Deflection Jacobian Formulation and Stent Delivery Algorithm

4.1 Deflection Jacobian Formulation. As shown in Fig. 10, the CTR of Fig. 3 has two portions: (I) precurved angle adjustment tube and (II) flexible surgical needle. Portion (I) is preformed in a circular shape. Portion (II) is straight and goes all the way through the support tube and portion (I). The contact force F is applied at the tip of portion (II).

Since our tube pair is a dominating case, we do not expect the force applied on portion (II) to affect the shape of portion (I). θ_{L1} is the deflection angle of portion (I) at point A, and θ_{L2} is the deflection angle of portion (II) at point B. The relative deflection of portion (II) with respect to portion (I) is calculated as $\theta_{L2} - \theta_{L1}$. The $\hat{\mathbf{x}}_O$–$\hat{\mathbf{y}}_O$ coordinate system is attached to the support tube such that $\hat{\mathbf{x}}_O$-direction is along the extension of the CTR. The $\hat{\mathbf{x}}_T$–$\hat{\mathbf{y}}_T$ coordinate system is attached to the tissue surface such that $\hat{\mathbf{x}}_T$ is along and $\hat{\mathbf{y}}_T$ is normal to the tissue surface. Local frames are also defined at points A and B such that $\hat{\mathbf{x}}_A$ and $\hat{\mathbf{x}}_B$ are along the tangent of the tubes and $\hat{\mathbf{y}}_A$ and $\hat{\mathbf{y}}_B$ are perpendicular to the tangent.

For a single cantilever beam with force applied at the free end, we have

$$x(l, t_L, t_F) = \int_0^l \cos(\theta(s, t_L, t_F))\, ds \tag{12}$$

$$y(l, t_L, t_F) = \int_0^l \sin(\theta(s, t_L, t_F))\, ds \tag{13}$$

where x and y denote the Cartesian coordinates of point B, l is the length of the beam, and $\theta(s, t_L, t_F)$ is given by Eq. (11). The relative velocity components of point B with respect to point A are found using Leibniz integral rule while using $\frac{\partial}{\partial t}(\theta_L) = 0$ and $\frac{\partial}{\partial t}(n_F) = 0$ since the Jacobian is a first-order Taylor expansion of the beam kinematics and the external load is assumed constant at a given time instant.

Table 1 Computation time comparison between interpolation and elliptic integral solutions

Beam loading and deflection conditions	Interpolation method Computation time (s)	Elliptic integral method Computation time (s)
$\theta_L = 10$ deg, $n_F = 0.0$–1.0 (0 deg–45 deg)	0.000168–0.000169	1.146652–1.192039
$\theta_L = 20$ deg, $n_F = 0.00$–1.0 (0 deg–45 deg)	0.000175–0.000177	1.174579–1.219528
$\theta_L = 30$ deg, $n_F = 0.00$–1.0 (0 deg–45 deg)	0.000182–0.000184	1.184637–1.267751
$\theta_L = 40$ deg, $n_F = 0.00$–1.0 (0 deg–45 deg)	0.000185–0.000186	1.139708–1.202666
$\theta_L = 50$ deg, $n_F = 0.00$–1.0 (0 deg–45 deg)	0.000209–0.000212	1.154969–1.237972

$$\dot{x}(l,t_L,t_F) = \cos(\theta(l,t_L,t_F))\,\dot{l} \tag{14}$$

$$\dot{y}(l,t_L,t_F) = \sin(\theta(l,t_L,t_F))\,\dot{l} \tag{15}$$

The deflection Jacobian of the cantilever beam is

$$\begin{bmatrix}\dot{x}(l,t_L,t_F)\\ \dot{y}(l,t_L,t_F)\end{bmatrix} = \mathbf{J}_D\,\dot{l} \quad \text{where} \quad \mathbf{J}_D = \begin{bmatrix}\cos(\theta(l,t_L,t_F))\\ \sin(\theta(l,t_L,t_F))\end{bmatrix} \tag{16}$$

For the CTR of Fig. 10, the velocity of point B is

$${}^{\mathrm{O}}\mathbf{v}_{\mathrm{B/O}} = {}^{\mathrm{O}}\mathbf{R}_{\mathrm{A}}\,{}^{\mathrm{A}}\mathbf{v}_{\mathrm{B/A}} + {}^{\mathrm{O}}\boldsymbol{\omega}_{\mathrm{A}} \times {}^{\mathrm{O}}\mathbf{R}_{\mathrm{A}}\,{}^{\mathrm{A}}\mathbf{p}_{\mathrm{B/A}} \tag{17}$$

where ${}^{\mathrm{A}}\mathbf{v}_{\mathrm{B/A}}$ and ${}^{\mathrm{A}}\mathbf{p}_{\mathrm{B/A}}$ denote the relative velocity and position of point B with respect to point A as described in local frame A. ${}^{\mathrm{O}}\mathbf{R}_{\mathrm{A}}$ is the rotation matrix about the z axis with the angle of rotation equal to θ_{L1}. ${}^{\mathrm{O}}\boldsymbol{\omega}_{\mathrm{A}} = \begin{bmatrix}0 & 0 & \dot{l}_{\mathrm{I}}/r_{\mathrm{I}}\end{bmatrix}^{\mathrm{T}}$ where $\dot{l}_{\mathrm{I}}$ is the extension speed of tube portion (I) and r_{I} is the radius of the circular precurved tube. Throughout this paper, bolded lowercase letter denotes vectors and bolded capitalized letter denotes matrix. The velocity of point B relative to point A is

$${}^{\mathrm{A}}\mathbf{v}_{\mathrm{B/A}} = \begin{bmatrix}\cos(\theta_{L2}-\theta_{L1})\\ \sin(\theta_{L2}-\theta_{L1})\\ 0\end{bmatrix}\dot{l}_{\mathrm{II}} \tag{18}$$

where $\dot{l}_{\mathrm{II}}$ is the insertion speed of tube portion (II).

The deflection Jacobian for the CTR is derived as

$${}^{\mathrm{O}}\mathbf{v}_{\mathrm{B/O}} = \mathbf{J}_{\mathrm{CTR}}\begin{bmatrix}\dot{l}_{\mathrm{I}}\\ \dot{l}_{\mathrm{II}}\end{bmatrix} = \mathbf{J}_{\mathrm{CTR}}\dot{\mathbf{l}} \text{ where}$$

$$\mathbf{J}_{\mathrm{CTR}} = \begin{bmatrix}\dfrac{-y_{\mathrm{B/A}}}{r_{\mathrm{I}}} & \cos(\theta_{L1})\cos(\theta_{L2}-\theta_{L1}) - \sin(\theta_{L1})\sin(\theta_{L2}-\theta_{L1})\\ \dfrac{x_{\mathrm{B/A}}}{r_{\mathrm{I}}} & \sin(\theta_{L1})\cos(\theta_{L2}-\theta_{L1}) + \cos(\theta_{L1})\sin(\theta_{L2}-\theta_{L1})\\ 0 & 0\end{bmatrix} \tag{19}$$

Using trigonometric functions to simplify Eq. (19) yields

$$\mathbf{J}_{\mathrm{CTR}} = \begin{bmatrix}\dfrac{-y_{\mathrm{B/A}}}{r_{\mathrm{I}}} & \cos(\theta_{L2})\\ \dfrac{x_{\mathrm{B/A}}}{r_{\mathrm{I}}} & \sin(\theta_{L2})\\ 0 & 0\end{bmatrix} \tag{20}$$

Equation (20) shows that the Jacobian of the CTR only depends on the absolute deflection angle at point B and the relative position of point B with respect to point A. Since tube portion (I) assumes a circular shape and is controlled by the user, the position of point A is known. Hence, for surgical applications, a visual position tracker is needed to read the position and orientation of frame B so that the Jacobian can be calculated in real time. While visual tool tracking is not the focus of our study, other groups have proven the feasibility of using stereo cameras for tool tracking in ophthalmic surgery [31].

4.2 Robot Control Algorithm. Potential applications of the proposed CTR include drug delivery, cannulation, and microvascular stenting. For these applications, the sharp tip of the CTR is used as a needle to poke through the top surface of the blood vessel. Next steps after the poking include orienting the CTR and advancing the guide wire. A resolved-rates algorithm is presented to address these two procedures.

The CTR is to be mounted to a carrying robot, whose end effector (EE) point coincides with point O in Fig. 10. The velocity relationship is derived as

$$\mathbf{v}_{\mathrm{B}} = \mathbf{v}_{\mathrm{O}} + \omega_{\mathrm{O}} \times {}^{W}\mathbf{R}_{\mathrm{O}}\,{}^{\mathrm{O}}\mathbf{p}_{\mathrm{B/O}} + {}^{W}\mathbf{R}_{\mathrm{O}}\,{}^{\mathrm{O}}\mathbf{v}_{\mathrm{B/O}} \tag{21}$$

In Eq. (21), ${}^{W}\mathbf{R}_{\mathrm{O}}$ represents the rotation matrix from the world frame to the EE frame of the carrying robot. Assume the carrying robot has Jacobian $\mathbf{J}_R$, we have

$$\mathbf{v}_{\mathrm{B}} = [\mathbf{I}_{3\times3}\ \ \mathbf{0}_{3\times3}]\mathbf{J}_R\dot{\mathbf{q}}_R + ([\mathbf{0}_{3\times3}\ \ \mathbf{I}_{3\times3}]\mathbf{J}_R\dot{\mathbf{q}}_R) \times \mathbf{p}_{\mathrm{B/O}} + {}^{W}\mathbf{R}_{\mathrm{O}}\mathbf{J}_{\mathrm{CTR}}\dot{\mathbf{l}} \tag{22}$$

where $\dot{\mathbf{q}}_R$ represents the joint rates of the carrying robot. Writing Eq. (22) in matrix form results in

$$\mathbf{v}_{\mathrm{B}} = \left[\underbrace{\left([\mathbf{I}_{3\times3}\ \ \mathbf{0}_{3\times3}] - \left[\mathbf{p}_{\mathrm{B/O}}\times\right][\mathbf{0}_{3\times3}\ \ \mathbf{I}_{3\times3}]\right)\mathbf{J}_R}_{\mathbf{J}_{\dot{q}_R}}\ \underbrace{{}^{W}\mathbf{R}_{\mathrm{O}}\mathbf{J}_{\mathrm{CTR}}}_{\mathbf{J}_{\mathrm{i}}}\right]\begin{bmatrix}\dot{\mathbf{q}}_R\\ \dot{\mathbf{l}}\end{bmatrix} \tag{23}$$

where $\left[\mathbf{p}_{\mathrm{B/O}}\times\right]$ denotes the cross-product matrix of $\mathbf{p}_{\mathrm{B/O}}$.

In the procedure of orienting the CTR, the CTR tip is fixed in position, while its orientation is adjusted to be parallel to the blood vessel channel. Therefore, $\mathbf{v}_{\mathrm{B}} = \mathbf{0}$ and we have

$$\mathbf{J}_{\mathrm{i}}\dot{\mathbf{l}} = -\mathbf{J}_{\dot{q}_R}\dot{\mathbf{q}}_R \tag{24}$$

A resolved-rate control method is used until the poking needle is parallel to the blood vessel channel ($\hat{\mathbf{x}}_{\mathrm{A}} = \hat{\mathbf{x}}_{\mathrm{T}}$), as defined in Eq. (25):

$$\theta_{L1} = \mathrm{Atan2}(\hat{\mathbf{x}}_{\mathrm{T}} \cdot \hat{\mathbf{y}}_{\mathrm{O}}, \hat{\mathbf{x}}_{\mathrm{T}} \cdot \hat{\mathbf{x}}_{\mathrm{O}}) \tag{25}$$

In the procedure of advancing the guide wire into the blood vessel, $\mathbf{v}_{\mathrm{B}}$ should be only along $\hat{\mathbf{x}}_{\mathrm{T}}$ and we have

$$(\mathbf{v}_{\mathrm{B}} \cdot \hat{\mathbf{x}}_{\mathrm{T}})\,\hat{\mathbf{x}}_{\mathrm{T}} = \begin{bmatrix}\mathbf{J}_{\dot{q}_R} & \mathbf{J}_{\mathrm{i}}\end{bmatrix}\begin{bmatrix}\dot{\mathbf{q}}_R\\ \dot{\mathbf{l}}\end{bmatrix} \tag{26}$$

Equation (26) provides the control strategy of assisted stent deployment. During assisted-stent deployment operation mode, it is assumed that the surgeon controls the advancement speed of the guide wire $\dot{\mathbf{l}}$, while the low-level controller of the slave robot controls the joint speeds $\dot{\mathbf{q}}_R$ such that insertion speed $v_{\mathrm{insertion}} = \mathbf{v}_{\mathrm{B}} \cdot \hat{\mathbf{x}}_{\mathrm{T}}$ is achieved without violating kinematic constraints of the incision points of the eye as specified in Ref. [25].

$$\dot{\mathbf{q}}_R = \mathbf{J}_{\dot{q}_R}^{-1}\left(v_{\mathrm{insertion}}\,\hat{\mathbf{x}}_T - \mathbf{J}_{\mathrm{i}}\dot{\mathbf{l}}\right) \tag{27}$$

While Eq. (27) provides a means for a resolved-rates control, it suffers from sensitivity to kinematic and integration errors. A closed-loop feedback using visual servoing is outside the scope of this paper but is a possible way to overcome this drawback.

5 Force Sensing

In retinal surgery, surgeons perform highly delicate operations on the retina without force feedback. They rely on visual cues and experience for guarding against damage to the retina. This sensory deficiency stems from the minute contact forces between the surgical tools and the retina (on the order of 20 mN for vessel puncture applications [33]). These forces are usually masked by larger friction forces between the surgical instruments and the access ports in the sclera. As a result, there is a need for a means to sense the forces inside the ocular cavity, but the unavailability of such tiny force sensors requires alternative approaches for force sensing.

The tubing robot proposed in Fig. 3 has the potential to provide contact force information to surgeons. In Sec. 3.3, the beam end point coordinates were calculated using an interpolation approach

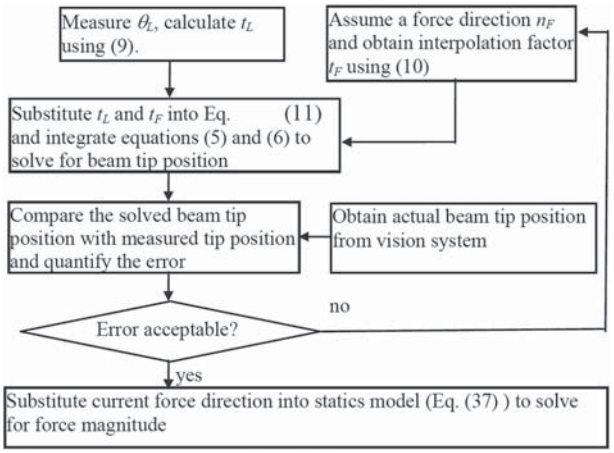

Fig. 11 Flowchart of the force sensing algorithm

for given force direction and deflection angle of the beam. For force sensing, assuming the deflection angle and the beam end point coordinates are given, a root-searching method can be used to determine the force direction and its magnitude.

Assume that the applied force direction on the free end of the beam satisfies Eq. (8). By using interpolation on the intermediate deflection angles of the reference beams defined in Fig. 8, and by integrating along the target beam curve, the entire interval of $[n_{F\min}, n_{F\max}]$ is scanned such that the value of n_F that minimizes the distance between the integrated beam end point and the observed beam end is recorded. This value of n_F is taken as the direction of the applied force, which is further substituted into the statics model (Eq. (A9) in the Appendix) to solve for the magnitude of the force. A flowchart of the algorithm is described in Fig. 11.

A numerical simulation was carried out to illustrate this algorithm. Figure 12 shows the simulation setup used to mimic the ophthalmic surgical procedures. The approach angle of the tubing robot, defined as the relative angle between the flexible needle when it is straight and the environment, is selected as 30 deg. The deflection interval of the flexible needle is therefore [0 deg, 30 deg]. The applied force direction interval is assumed to be $[\tan(\pi/6), \tan(\pi/3)]$. The length of the needle is 5 mm, and the Young's modulus and the moment of inertia of the needle are 57.85 GPa and $1.18 \times 10^{-18}\text{m}^4$, respectively. These parameters are selected to simulate our target application of microstenting in retinal surgery.

Assume the target beam end point coordinates are measured as (4.84 mm, 1.14 mm) and that the deflection angle is 20 deg. By minimizing the distance between the integrated beam end point

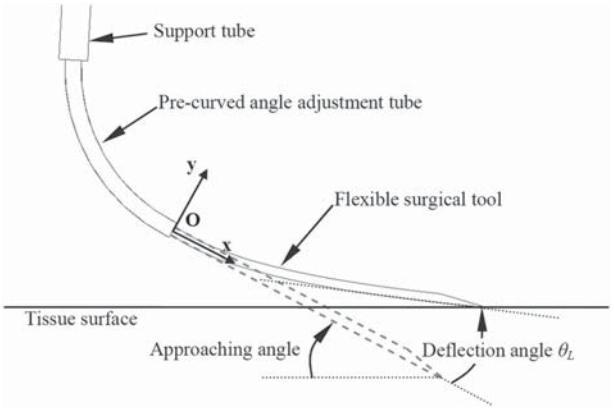

Fig. 12 Illustration of the proposed surgical setup for the robot

Table 2 Comparison of force sensing versus theoretical calculation

	Force sensing results	Theoretical results
Force direction	$n_F = 1.43$ (55.1 deg)	$n_F = 1.50$ (56.3 deg)
Force magnitude	2.44 mN	2.49 mN

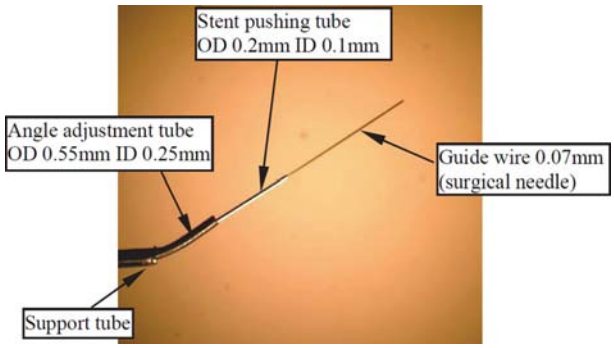

Fig. 13 Proposed 3-DoF tubing robot

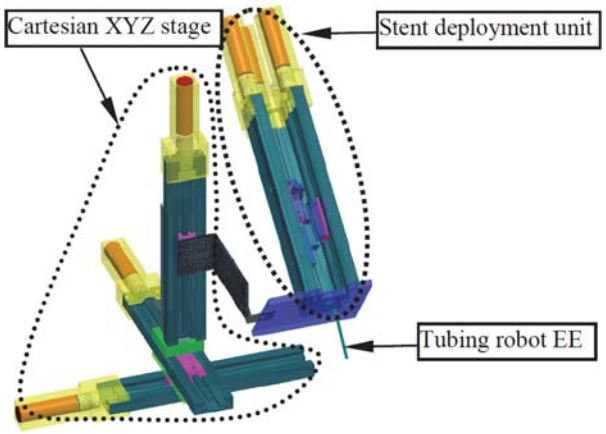

Fig. 14 CAD model of the tubing robot and the carrying robot

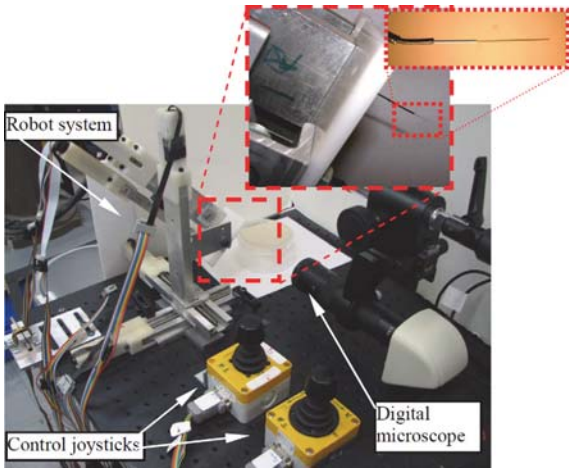

Fig. 15 Experimental setup of the system

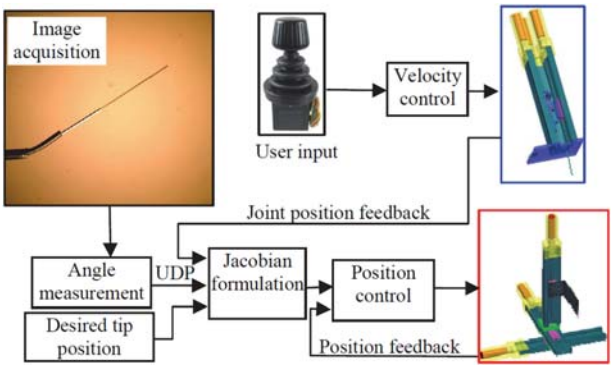

Fig. 16 Control architecture used for the stenting experiment

and the observed position, optimal n_F is calculated as 1.43 and the force magnitude is calculated as 2.44 mN. These results are compared with the theoretical results solved from the elliptic integrals as in Table 2.

Table 2 shows that the force direction based on the force sensing algorithm has a 1.2 deg deviation from the theoretical results calculated from the elliptic integrals. Also, the force magnitude differs 0.05 mN from the nominal value, yielding an error of 2%. This error comes from the interpolation error as plotted in Fig. 9, where by integrating along the target beam, the resulting end point has a small offset compared with the actual beam end position. Considering the current situation associated with ophthalmic surgeries where surgeons have no force feedback at all, this error is acceptable. Moreover, the calculation time of implementing the entire force sensing algorithm was recorded in MATLAB® as 17 ms. It is fast enough to provide surgeons "real-time" force readings (over 50 readings per second) during a surgery.

6 Experimental Validation

A 3-DoF tubing robot shown in Fig. 13 was used for the experimental validation. All tubes of this robot were made from superelastic NiTi alloy according to the dimensions given in Sec. 2.2 and in Fig. 13. These dimensions were selected due to their suitability to adult human retinal veins, (approximately 0.16 mm as they exit the optic nerve head [34]). Same as in Fig. 4, this design targets applications such as stent delivery where a stent-pushing DoF was added to deliver the stent at the target site. For applications such as cannulation and drug delivery, a simplified 2-DoF design as shown in Fig. 3 is used.

The control unit of the tubing robot consists of three coaxially aligned linear actuators and a Cartesian XYZ stage, Fig. 14. The tubing robot EE as noted in Fig. 14 is observed under a digital microscope, as shown in Fig. 13.

6.1 Robot Coordinated Motion. For testing robot coordinated motion, an experimental setup was designed as shown in Fig. 15. A digital microscope was placed sideways to the tubing robot to measure its deflection. Two 3-DoF joysticks were used to control the XYZ stage and the tubing robot, respectively. In the experiment, the microscope acquired real-time images of the tubing robot and MATLAB® image processing toolbox were used to quantify the guide wire deflection angle during operation. By using MATLAB® xPC target toolbox with user datagram protocol (UDP) communication, the calculated deflection angle was sent to the target control machine for online update of the Jacobian formulation. The low-level position control loop was implemented using 1 KHz control frequency. The frequency of image acquisition, segmentation, deflection angle calculation, and UDP communication was 10 Hz.

As elaborated in Sec. 4.2, in a stent delivery procedure, two successive steps were needed to first adjust the tubing robot EE

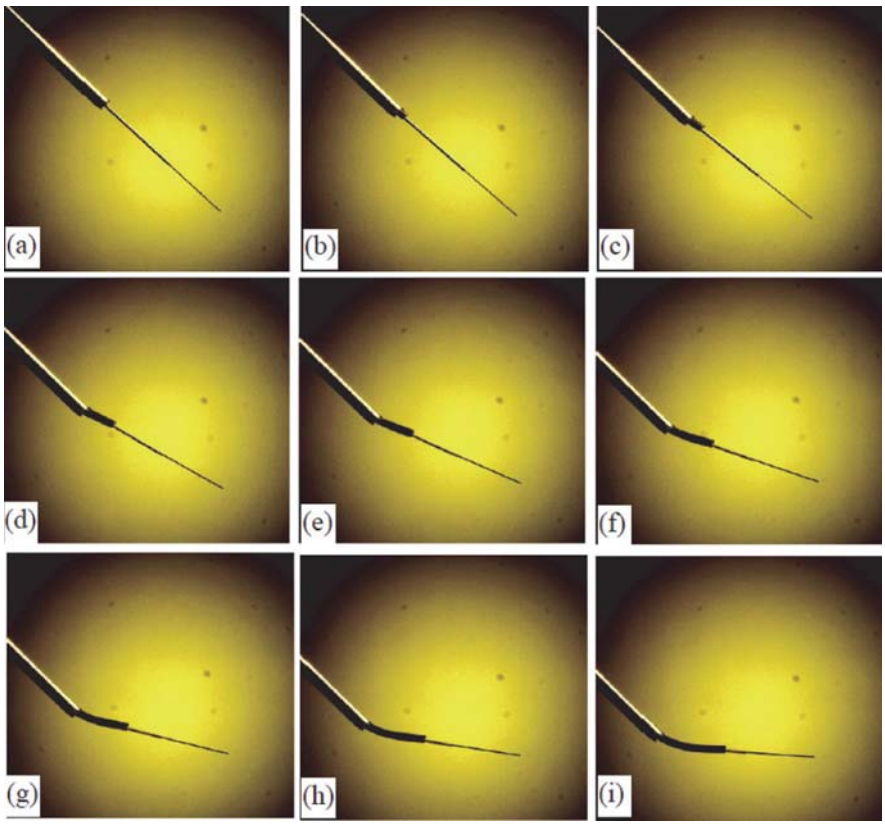

Fig. 17 Experimental image sequence to orient the tubing robot while maintaining its EE point position in the air

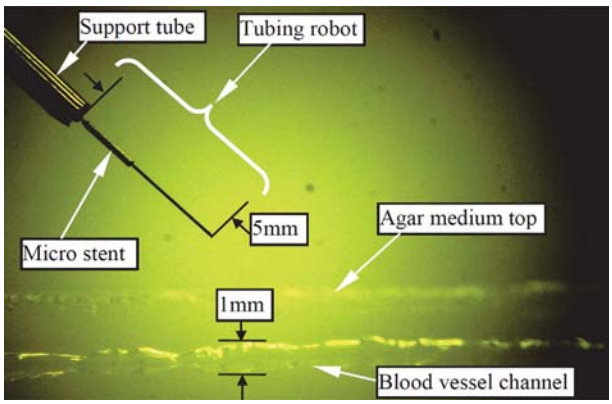

Fig. 18 Stent delivery experimental setup with artificial blood vessel channel created in agar

orientation and then advance the guide wire. This experiment was designed to demonstrate the ability of the robot to orient the tubing robot while maintaining its EE position in the air. The Jacobian formulation and direct kinematics were based on the interpolation method proposed in Sec. 3.

Figure 16 shows the control architecture for assistive stent deployment based on the formulation of Sec. 4. The insertion of the stent was carried out using the two operation modes discussed in Sec. 4.2 (operation mode I: orienting the guide wire while maintaining its tip position, and operation mode II: advancing the guide wire to the target site). In operation mode I, the user was able to adjust the angle of the guide wire using a 3-DoF analogue joystick (P3 America® Model 822) and velocity control. The *XYZ* stage was controlled using PID position control based on position feedback from the stenting unit and the *XYZ* stage. This feedback was used for updating the Jacobian of the robot based on the angle measurement via UDP communication. A desired reference tip position was given to the controller corresponding to each operation mode.

Figures 17(*a*)–17(*k*) show the experimental results as the angle adjustment tube was extended out from the support tube. Each image was taken by advancing the angle adjustment tube 0.5 mm. Throughout this experiment, the deflection angle of the guide wire was calculated and sent to the target control machine for online update of the Jacobian formulation. In Fig. 17, the stains on the microscope lens can be used as references for the robot EE tip position. The robot tip maximal error was measured as 0.5 mm.

In our actual Jacobian implementation for Eq. (24), we added a compensation matrix as in Eq. (28). This matrix corrected the

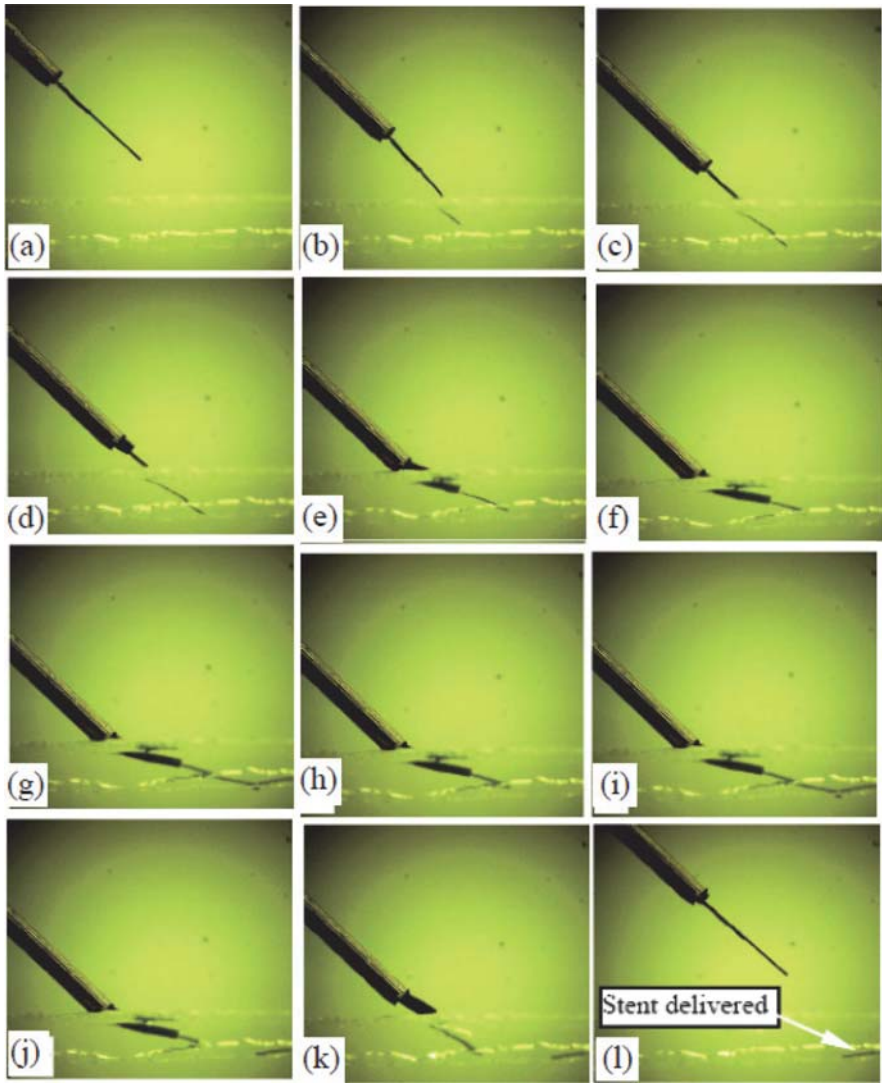

Fig. 19 Experimental image sequence for microstent delivery in agar-based blood vessel channel model

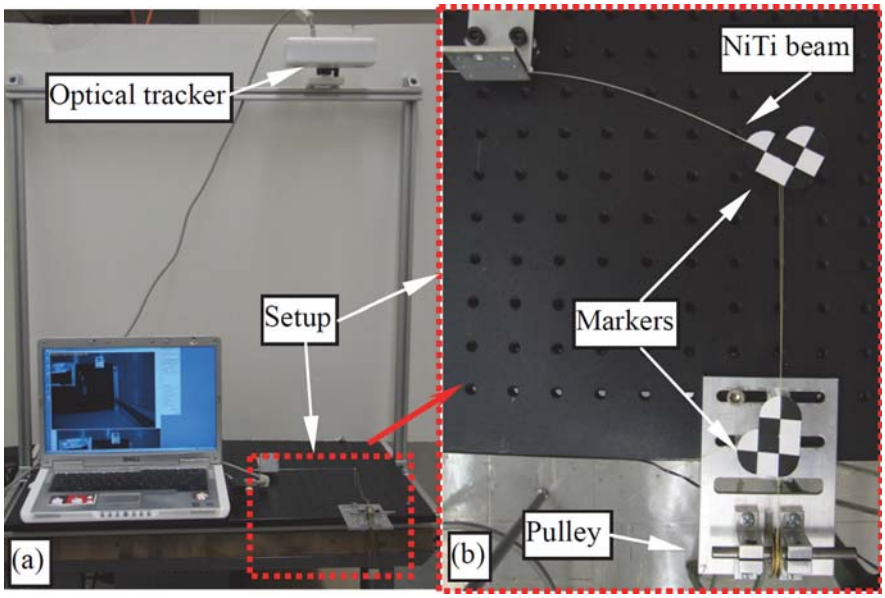

Fig. 20 Experimental setup for force sensing verification: (*a*) optical tracker tracing position and orientation of a cantilever beam tip and (*b*) loading setup to the cantilever beam tip

Table 3 Force sensing data compared to theoretical values

	Sensed force direction (deg)	Actual force direction (deg)	Sensed force magnitude (mN)	Actual load magnitude (mN)
1	13.6	15.0	117.3	118
2	24.1	21.3	115.8	118
3	28.9	30.0	117.1	118
4	35.6	37.5	119.2	118
5	36.4	44.0	116.2	118
6	19.6	16.8	116.1	118
7	22.4	24.3	119.0	118
8	31.6	33.8	119.4	118
9	36.0	41.3	117.7	118
10	46.2	47.2	117.9	118
11	23.2	15.7	114.1	118
12	24.3	24.3	117.9	118
13	33.1	33.4	119.5	118
14	37.2	41.0	118.6	118
15	44.9	48.0	117.0	118

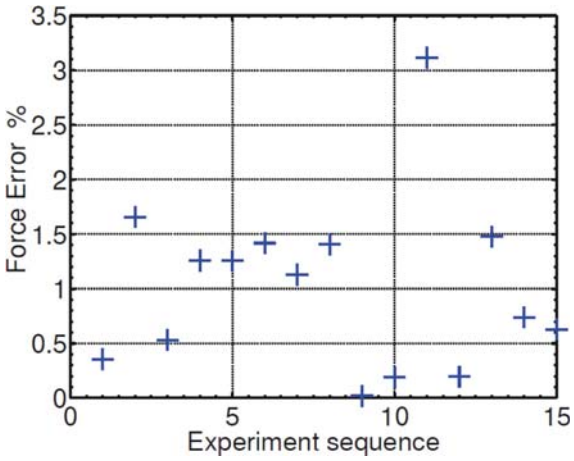

Fig. 21 Force sensing error plot

required motion from the XYZ stage along the x-axis to compensate for an observed deviation of the guide wire from the angle at the tip of the angle adjustment tube. This deviation is not accounted for in our idealized kinematic model, which assumes perfect alignment between the guide wire and the tip of the angle adjustment tube. Without the use of correction factors as in Eq. (28), the tip movement errors were close to 1.5 mm.

This compensation matrix was selected based on the series of experiments quantifying the tip error during tip movement as in Fig. 17. The correction parameters were easily found by the trial and error method based on the observation that the bore size of the angle adjustment tube was bigger than the outer diameter of the inner tube pair. This difference caused the inner tube pair to lean against the outer wall of the angle adjustment tube, Fig. 17(*e*). This resulted in a slight decrease in the actual angle of the guide wire. We note that this compensation matrix is equivalent to calibrating the robot parameter using a least squares approach based on vision feedback. With this implementation using Eq. (28), the position error of the robot tip lies within 0.5 mm. We note that the Velmex Unislide® linear slides used for the construction of the Cartesian XYZ stage had backlash of up to 0.2 mm. In future system implementation, a closed loop vision feedback will be used along with a precise parallel robot that will replace the Cartesian XYZ stage. All of these modifications are expected to further improve system performance.

$$\mathbf{J}'_{\mathbf{i}} = \begin{bmatrix} 0.75 & 0 & 0 \\ 0 & 1 & 0 \\ 0 & 0 & 1 \end{bmatrix} \mathbf{J}_{\mathbf{i}} \tag{28}$$

6.2 Stent Deployment. In this experiment, the tubing robot was used to deliver a stent at a target surgical site within an artificial blood vessel. The mockup stent was made from the same NiTi tube as the stent pushing tube, which had an OD of 0.2 mm and an ID of 0.1 mm. Mockup blood vessel channels of 1 mm diameter were created in agar, a material regularly used for artificial micro blood vessels, [35]. Figure 18 shows the experimental setup. The angle adjustment tube and the stent pushing tube were retracted into the support tube at their home configurations. The initial length of the guide wire that extended outside of the support tube was 5 mm. The microstent was pre-assembled to the guide wire. In a real application, the environment of the robot with

respect to the tissue inside the eye is similar. The robot approaches the tissue surface at a determined angle and then delivers the stent.

Figure 19 shows the stent delivery process. Figure 19(*a*) is identical to Fig. 18 and shows the initial setup. Figures 19(*b*) and 19(*c*) show the robot poking through the top surface of the blood vessel using velocity control of the XYZ stage. Figure 19(*d*) shows that the EE tip is already inside the blood vessel and the tubing robot is starting the angle adjustment using operation mode I. Figures 19(*d*)–19(*f*) show the angle adjustment process by extending the angle adjustment tube. This process is similar to the experiment A as illustrated in Fig. 17. Figure 19(*g*) shows the extension of the stent pushing tube to deliver the stent (operation mode II). Figure 19(*i*) shows that the stent has been delivered to the target site and Fig. 19(*j*) shows the retraction of the stent pushing tube. Figures 19(*k*) and 19(*l*) show the retraction process of the tubing robot from the blood vessel. It includes retracting the angle adjustment tube and raising the height of the entire tubing robot. At the end of this process, the stent remained inside the blood vessel after the guide wire was retracted.

6.3 Force Sensing Verification. As proposed in Sec. 5, the tubing robot can be used as a mechanical force sensor such that the contact force between the environment and the robot tip can be calculated. In this subsection, a force sensing experiment was designed for a larger-scale cantilever beam while subject to a force load applied at the tip. The reason for using a scaled-up beam was to allow us to measure the forces at the tip using an existing electronic scale in our lab. A setup with sub milliNewton resolution was required for the thin guide wire in Fig. 19 and it was not readily available.

Figure 20(*a*) shows the experimental setup where an optical tracker was used to record the position and orientation of the tubing robot tip. Figure 20(*b*) shows that the robot tip was loaded with weights via a thread and a frictionless pulley.

We selected a 100 mm long NiTi tube as the cantilever beam, with ID 0.76 mm and OD 0.89 mm. The Young's modulus of this specific tube was 57.85 GPa. As shown in Fig. 20(*b*), one marker was attached to the beam tip to record the position and deflection of the beam. A second marker was attached to the thread to record the loading force direction. By changing the position of the pulley, we were able to adjust the loading directions. Fifteen experiments were performed by changing the loading direction between 0 deg and 50 deg.

From Table 3, we see that although the sensed force direction differed from the theoretical readings by a maximum of 7.6 deg in experiment trial #5, the sensed force magnitude error was always less than 4% compared to our nominal value of 118 mN (12 g) (Fig. 21). Therefore, the feasibility of using the tubing robot as a mechanical force sensor for ophthalmic surgical procedures is verified.

7 Conclusion

This paper presented a unified framework for modeling large deflections of cantilever beams using polynomial approximation and linear interpolation. This modeling method did not require time-consuming iterative computation and was able to generate the entire beam shape for real-time control purposes. The modeling framework was extended to formulate the Jacobian of a novel tubing robot while subject to external loads at the tip. The robot was designed for assisting challenging ophthalmic surgical procedures such as retinal vascular stenting, for which two control modes were defined. The modeling method was further utilized for an online algorithm to sense the contact force between the robot and the tissue. Experimental results justified the Jacobian formulation, stent delivery operation, and force sensing algorithm. The methodology presented in this paper has the potential of enabling ophthalmic surgeons to perform demanding procedures while monitoring the applied force for safe operations.

Acknowledgment

Dr. Simaan was funded from NSF Career Grant IIS #1063750.

Appendix

A load applied to the free distal end generates nonlinear beam deflection, which is governed by the Bernoulli–Euler equation

$$M = EI\frac{d\theta}{ds} = EI\frac{\dfrac{d^2y}{dx^2}}{\left(1+\left(\dfrac{dy}{dx}\right)^2\right)^{3/2}} \tag{A1}$$

Howell [22] derived the elliptic integral solutions for the tip position of the deflected beam. Given a beam with a length l subject to a tip load as in Fig. 6, the tip coordinates (a,b) are given by

$$\begin{aligned}\frac{b}{l} &= \frac{1}{\alpha\eta^{5/2}}\begin{pmatrix}\eta\,[F(t)-F(\gamma,t)+2(E(\gamma,t)-E(t))]\\ +n\sqrt{2\eta(\eta+\lambda)}\cos(\gamma)\end{pmatrix}\\ \frac{a}{l} &= \frac{1}{\alpha\eta^{5/2}}\begin{pmatrix}-n\eta\,[F(t)-F(\gamma,t)+2(E(\gamma,t)-E(t))]\\ +\sqrt{2\eta(\eta+\lambda)}\cos(\gamma)\end{pmatrix}\end{aligned} \tag{A2}$$

where $F(t)$ and $E(t)$ are the elliptic integrals of the first and second kind. Parameters η, α, γ, λ, and t are given by

$$\eta = \sqrt{1+n^2} \tag{A3}$$

$$\lambda = \sin(\theta_L) - n\cos(\theta_L) \tag{A4}$$

$$\alpha = 1\Big/\sqrt{2}\int_0^{\theta_L} d\theta\Big/\sqrt{\lambda-\sin(\theta)+n\cos(\theta)} \tag{A5}$$

$$\gamma = \arcsin\left(\sqrt{(\eta-n)/(\eta+\lambda)}\right) \tag{A6}$$

$$t = \sqrt{(\eta+\lambda)/2\eta} \tag{A7}$$

Based on the functional dependence in Eqs. (A3)–(A7), we note that

$$t = t(\eta(n),\lambda(\theta_L)) \quad \gamma = \gamma(n,\eta(n),\lambda(\theta_L)) \quad \alpha = \alpha(\theta_L,t,n) \tag{A8}$$

So given a beam tip deflection angle θ_L and a force direction n, the force magnitude can be solved from the following equation:

$$P = \alpha^2\frac{EI}{l^2} \tag{A9}$$

This demonstrates that for a given beam tip angle and a force direction, the force magnitude is determined.

References

[1] Webster, R. J., Kim, J. S., Cowan, N. J., Chirikjian, G. S., and Okamura, A. M., 2006, "Nonholonomic Modeling of Needle Steering," Int. J. Robot. Res., **25**(5–6), pp. 509–525.

[2] Minhas, D., Engh, J., Fenske, M., and Riviere, C. N., 2007, "Modeling of Needle Steering Via Duty-Cycled Spinning," *28th Annual International Conference of IEEE Engineering in Medicine and Biology Society*, Lyon, France, pp. 2756–2759.

[3] Glozman, D., and Shoham, M., 2007, "Image-Guided Robotic Flexible Needle Steering," IEEE Trans. Robot., **23**(3), pp. 459–467.

[4] Okazawa, S., Ebrahimi, R., Chuang, J., Salcudean, S. E., and Rohling, R., 2005, "Hand-Held Steerable Needle Device," IEEE/ASME Trans. Mechatron., **10**(3), pp. 285–296.

[5] Sears, P., and Dupont, P., 2006, "A Steerable Needle Technology Using Curved Concentric Tubes," *IEEE/RSJ International Conference on Intelligent Robots and Systems*, Beijing, China, pp. 2850–2856.
[6] Webster, R. J., Okamura, A. M., and Cowan, N. J., 2006, "Toward Active Cannulas: Miniature Snake-Like Surgical Robots," *IEEE/RSJ International Conference on Intelligent Robots and Systems*, Beijing, China, pp. 2857–2863.
[7] Jones, B. A., Gray, R. L., and Turlapati, K., 2009, "Three Dimensional Statics for Continuum Robotics," *IEEE/RSJ International Conference on Intelligent Robots and Systems*, St. Louis, pp. 2659–2664.
[8] Webster, R. J., Romano, J. M., and Cowan, N. J., 2009, "Mechanics of Precurved-Tube Continuum Robots," IEEE Trans. Rob., **25**(1), pp. 67–78.
[9] Rubin, M. B., and Tufekci, E., 2005, "Three-Dimensional Free Vibrations of a Circular Arch Using the Theory of a Cosserat Point," J. Sound Vib., **286**, pp. 799–816.
[10] Sears, P., and Dupont, P., 2007, "Inverse Kinematics of Concentric Tube Steerable Needles," *IEEE International Conference on Robotics and Automation*, Rome, Italy, pp. 1887–1892.
[11] Alterovitz, R., Branicky, M., and Goldberg, K., 2008, "Motion Planning Under Uncertainty for Image-Guided Medical Needle Steering," Int. J. Robot. Res., **27**(11–12), pp. 1361–1374.
[12] Park, W., Liu, Y., Zhou, Y., Moses, M., and Chirikjian, G. S., 2008, "Kinematic State Estimation and Motion Planning for stochastic Nonholonomic Systems Using the Exponential Map," Robotica, **26**(4), pp. 419–434.
[13] Kallem, V., and Cowan, N. J., 2009, "Image Guidance of Flexible Tip-Steerable Needles," IEEE Trans. Robot., **25**(1), pp. 191–196.
[14] Mahvash, M., and Dupont, P., 2008, "Bilateral Teleoperation of Flexible Surgical Robots," *IEEE International Conference on Robotics and Automation, Workshop on New Vistas and Challenges in Telerobotics*, Pasadena, CA, pp. 58–64.
[15] Xu, K., and Simaan, N., 2010, "Analytic Formulation for Kinematics, Statics and Shape Restoration of Multi-Backbone Continuum Robots via Elliptic Integrals," ASME J. Mech. Robot., **2**(1), pp. 011006(1–13).
[16] Kimball, C., and Tsai, L.-W., 2002, "Modeling of Flexural Beams Subjected to Arbitrary End Loads," ASME J. Mech. Des., **124**(2), pp. 223–234.
[17] Goksel, O., Dehghan, E., and Salcudean, S. E., 2009, "Modeling and Simulation of Flexible Needles," Med. Eng. Phys., **31**, pp. 1069–1078.
[18] Wang, X., and Mills, J. K., 2005, "Dynamic Modeling of a Flexible-Link Planar Parallel Platform Using a Substructuring Approach," Mech. Mach. Theory, **41**(6), pp. 671–687.
[19] Wakamatsu, H., and Hirai, S., 2004, "Static Modeling of Linear Object Deformation Based on Differential Geometry," Int. J. Robot. Res., **23**(3), pp. 293–311.
[20] Wang, J., Chen, J.-K., and Liao, S., 2008, "An Explicit Solution of the Large Deformation of a Cantilever Beam Under Point Load at the Free Tip," J. Comput. Appl. Math., **212**, pp. 320–330.
[21] Shvartsman, B. S., 1999, "Direct Method for Analysis of Flexible Beam Under a Follower Load," *Proceedings of Computational of Mechanics for the Next Millennium*, Singapore, pp. 155–160.
[22] Howell, L. L., 2001, *Compliant Mechanisms*, Wiley, New York.
[23] Su, H.-J., 2009, "A Pseudo-rigid-Body 3R Model for Determining Large Deflection of Cantilever Beams Subject to Tip Loads," ASME J. Mech. Robot., **1**(2), p. 021008.
[24] Fertis, D. G., 1999, *Nonlinear Mechanics*, CRC, Boca Raton.
[25] Wei, W., Goldman, R. E., Fine, H. F., Chang, S., and Simaan, N., 2009, "Performance Evaluation for Multi-Arm Manipulation of Hollow Suspended Organs," IEEE Trans. Rob., **25**(1), pp. 147–157.
[26] Stewart, D., 1965, "A Platform With 6 Degrees of Freedom," Proceedings of the Institution of Mechanical Engineers.
[27] Bynoe, L. A., and Weiss, J. N., 2003, "Retinal Endovascular Surgery and Intravitreal Triamcinolone Acetonide for Central Vein Occlusion in Young Adults," Am. J. Ophthalmol., **135**(3), pp. 382–384.
[28] Weiss, J. N., 1998, "Treatment of Central Retinal Vein Occlusion by Injection of Tissue Plasminogen Activator into A Retinal Vein," Am. J. Ophthalmol., **126**(1), pp. 142–144.
[29] Weiss, J. N., 2000, "Retinal Surgery for Treatment of Central Retinal Vein Occlusion," Ophthalmic Surgery Lasers, **31**(2), pp. 162–165.
[30] Weiss, J. N., and Bynoe, L. A., 2001, "Injection of Tissue Plasminogen Activator into A Branch Retinal Vein in Eyes With Central Retinal Vein Occlusion," Ophthalmology, **108**(12), pp. 2249–2257.
[31] Dewan, M., Marayong, P., Okamura, A. M., and Hager, G. D., 2004, "Vision-Based Assistance for Ophthalmic Micro-Surgery," *7th International Conference on Medical Image Computing and Computer-Assisted Intervention (MICCAI)*, Springer, Rennes, Saint-Malo, France, pp. 49–57.
[32] Paul, R. P., 1981, *Robot Manipulators: Mathematics, Programming, and Control*, The MIT Press, Cambridge, MA.
[33] Jagtap, A., and Riviere, C. N., 2004, "Applied Force during Vitreoretinal Microsurgery With Handheld Instruments," *26th Annual International Conference of the Engineering in Medicine and Biology Society*, San Francisco, CA, pp. 2771–2773.
[34] Leng, T., Miller, J. M., Bilbao, K. V., Palanker, D. V., Huie, P., and Blumenkranz, M. S., 2004, "The Chick Chorioallantoic Membrane as a Model Tissue for Surgical Retinal Research and Simulation," Retina, **24**(3), pp. 427–434.
[35] LoRusso, F. J., and Font, R. L., 1999, "Use of Agar in Ophthalmic Pathology: A Technique to Improve the Handling and Diagnosis of Temporal Artery Biopsies, Subfoveal Membranes, Lens Capsules, and Other Ocular Tissues," Ophthalmology, **106**(11), pp. 2106–2108.